

Article pubs.acs.org/crystal

Morphology Control of Self-Assembled Three-Phase Au-BaTiO₃— ZnO Hybrid Metamaterial for Tunable Optical Properties

Shikhar Misra, Di Zhang, Zhimin Qi, Dongfang Li, Juanjuan Lu, Hou-Tong Chen, and Haiyan Wang*

Article Recommendations



10 Permittivity(E) 995nm 678nm -5 20 nm 20 nm -10 1000 1250 500 750 Wavelength (nm)

ABSTRACT: Microstructural control in metal-dielectric hybrid metamaterials presents enormous opportunities in tailoring the physical properties including the magnetic and optical properties. Here, we demonstrate a strong tunability achieved in the microstructure of self-assembled ordered three-phase Au-BaTiO₃-ZnO hybrid metamaterial along with its optical properties, grown by a pulsed laser deposition method. Varying the growth temperature, deposition frequency, and template thickness evolves the microstructure by tuning the Au and ZnO pillar geometry as well as the shape and size of the Au nanoparticles capping the ZnO nanowires. The three-phase hybrid metamaterials exhibit unique optical properties, including enhanced nonlinear optical properties, hyperbolic dispersion in the visible and near-infrared wavelength region, and tuned epsilon-near-zero (ENZ) wavelength upon varying the deposition parameters. This study suggests that the three-phase hybrid metamaterials present great potential in the microstructure and optical property tuning that can also be applied to other two-phase and three-phase nanocomposite systems.

INTRODUCTION

Metal-dielectric nanocomposites as hybrid metamaterials have demonstrated a variety of physical properties and multifunctionalities toward practical applications in magnetic storage devices, photocatalysts, waveguides, smart windows, batteries, and optical metamaterials. The anisotropic nature of these nanocomposites is usually achieved by fabricating them in either multilayer or nanowire morphology using a two-phase nanocomposite approach.^{3,8-14} The hybrid materials with either metallic phase embedded inside the oxide matrix as vertical pillars or alternatively stacked in a multilayer design show very strong anisotropic physical properties, ideal for applications such as subdiffraction imaging, negative refraction, and optical magnetism. 15-18 For example, a Au/Al₂O₃ multilayer structure with a periodic hole array through the film stack has shown a negative index at near-IR frequencies, while a Au/BaTiO3 system with periodic Au nanowires embedded in BaTiO₃ matrix shows hyperbolic dispersion in the near-IR wavelength region. 12,18

Very recently, a group of hybrid metamaterials in a unique oxide-metal vertically aligned nanocomposite (VAN) form has been demonstrated using pulsed laser deposition

(PLD). 10,12,19-22 The nanocomposites act as a hyperbolic metamaterial for wavelengths longer than the epsilon-near-zero (ENZ) wavelength due to its anisotropic morphology, behaving as a metal in one axis (ε_z < 0) and a dielectric in the other axes ($\varepsilon_x = \varepsilon_y > 0$). Such hyperbolic metamaterials support the propagation of high wavevectors which provide a multifunctional platform for realizing subdiffraction limited imaging, nanolithography, and ultrasensitive optical sensing devices. 16,23-27 In addition, tuning the effective electromagnetic response of the hyperbolic metamaterials by varying the ENZ wavelength is technologically important for realizing a nonlinear material response in different wavelength regions.^{28,29} Such an ENZ wavelength tunability can be achieved by varying the aspect ratio and density of the metallic phase as

Supporting Information

Received: June 11, 2020 Revised: July 15, 2020 Published: July 15, 2020





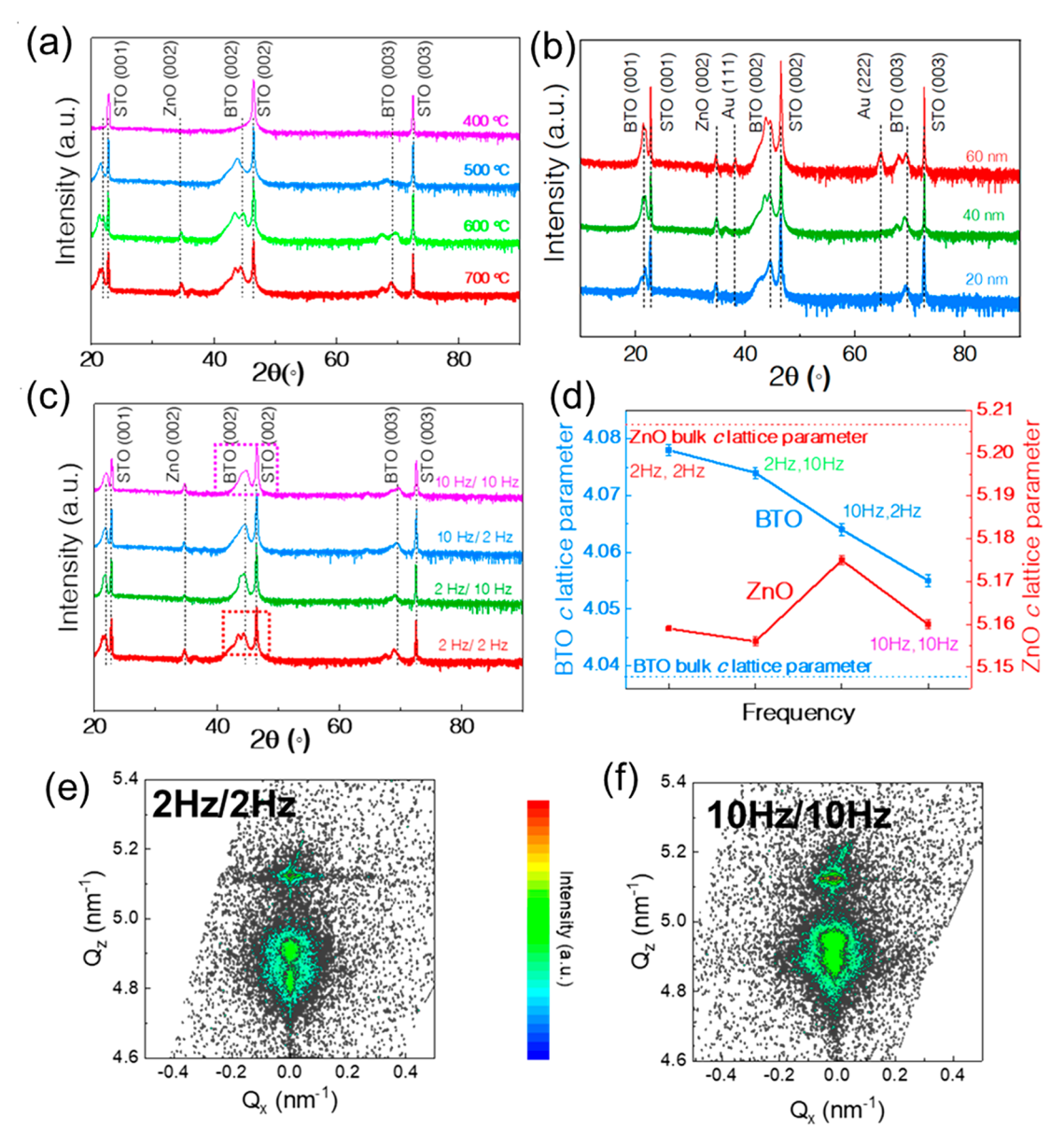


Figure 1. X-ray diffraction of the ordered three-phase Au-BaTiO₃–ZnO nanocomposite thin films. XRD plots dependent on deposition parameters (a) temperature, (b) Au-BaTiO₃ template thickness, and (c) frequency. (d) c lattice parameter of BaTiO₃ and ZnO plotted at different deposition frequencies, deposited on SrTiO₃ (STO) (001) substrate. (e–f) Reciporocal space maps (RSM) around the STO (002) peak for the 2 Hz/2 Hz and 10 Hz/10 Hz samples, respectively.

shown in two-phase systems including Au-BaTiO₃(Au-BTO) and Au-ZnO. ^{9,21} In these studies, careful microstructural control modulates the free electron density in the out-of-plane direction, thereby tuning the hyperbolic dispersion characteristics of the metal-dielectric nanocomposites. To achieve multifunctionalities and complex geometry designs for developing next generation integrated electronic and photonic devices, a third phase has been incorporated into a two-phase nanocomposite to form a three-phase nanocomposite design, such as the self-assembled ordered Au-BaTiO₃–ZnO (Au-BTO-ZnO) with coupled ferroelectric property and hyperbolic dispersion in the visible and near-infrared wavelength region. ³⁰ Such three-phase systems provide additional degrees of freedom in providing morphological and functional tunabilities.

In this work, we demonstrate the tunable morphology of the Au-BTO-ZnO three-phase nanocomposite, by varying the

deposition parameters using a two-step PLD process. The twostep PLD includes the first layer deposition of the Au-BTO template followed by the second layer deposition of the BTO-ZnO nanocomposite. This produces a unique complex and highly ordered three-phase nanocomposite structure. Different deposition parameters, including the growth temperature, template (the first layer of Au-BTO) thickness, deposition frequency, and the underlying substrate selected (SrTiO₃(STO), MgO and LaAlO₃ (LAO)), were applied and gave rise to distinct microstructures. On the other hand, the parameter dependent study also provides fundamental understanding of the growth mechanism, driven by thermodynamics and growth kinetics of the self-assembly process. Detailed microstructural analysis including X-ray diffraction (XRD), (scanning) transmission electron microscopy (S)TEM coupled with energy-dispersive X-ray spectroscopy (EDS) elemental mapping has been conducted to correlate with the optical

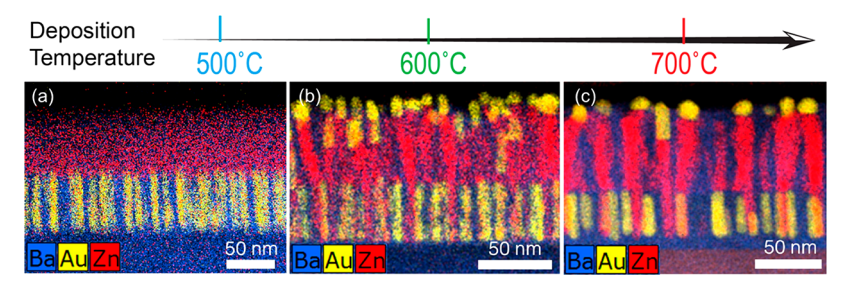


Figure 2. Cross-sectional EDS elemental maps of the three-phase Au-BaTiO₃–ZnO nanocomposite thin films, deposited at (a) 500 $^{\circ}$ C, (b) 600 $^{\circ}$ C, and (c) 700 $^{\circ}$ C on STO (001) substrate.

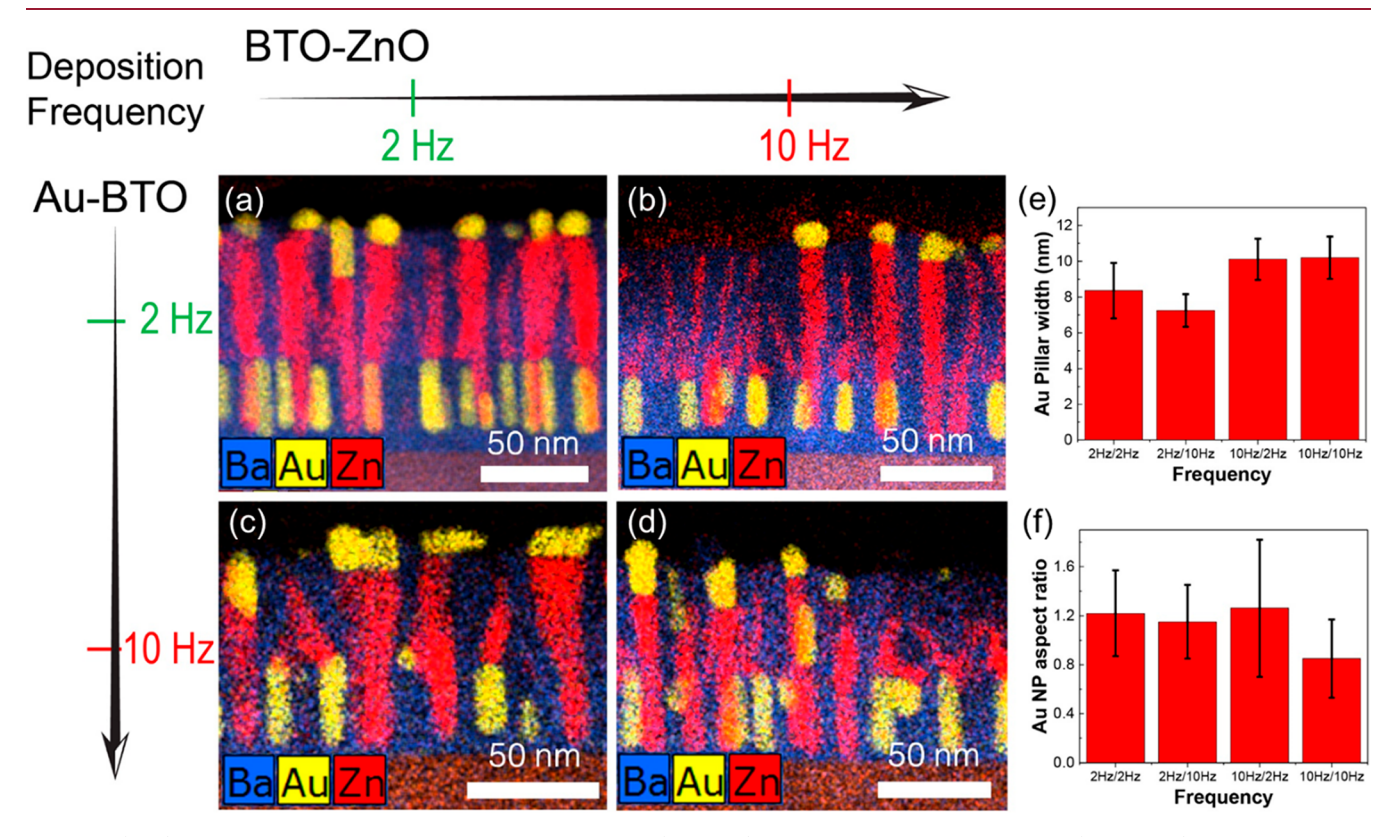


Figure 3. (a–d) Cross-sectional EDS elemental maps of Au-BaTiO₃ (Au-BTO) template layer and $BaTiO_3$ –ZnO (BTO-ZnO) layer, deposited on the STO (001) substrate at different deposition frequencies. (e) Plot of the Au pillar width and (f) Au nanoparticle aspect ratio at different deposition frequencies.

properties, including the complex dielectric properties and hyperbolic properties, especially the ENZ wavelength in the visible and near-infrared wavelength regions.

■ RESULTS AND DISCUSSION

All of the three-phase Au-BTO-ZnO samples were deposited using a two-step templating growth method (see Experimental Details). Figure 1 shows a collection of XRD graphs for the three-phase Au-BTO-ZnO at various growth temperatures, template thicknesses, and frequencies to determine the growth orientation and strain relaxation in the films on single-crystalline STO (001) substrates. Figure 1a shows the XRD plots for the temperature dependent samples deposited at 400, 500, 600 and 700 °C. BTO and ZnO texture along [002] and [0002], respectively. The BTO (002) peak shows a splitting that corresponds to the different strain states in the BTO. Both the BTO and ZnO peaks completely disappear for the 400 °C sample, implying that the crystallinity of the film reduces at low growth temperatures. Figure 1b shows the XRD plots with

different bottom Au-BTO template layer thicknesses. The template thickness was varied from 20 nm to 60 nm. Interestingly, the peak splitting in BTO can be attributed to the lower (Au-BTO) and upper (BTO-ZnO) layers, respectively. The bottom BTO layer is constrained by the STO substrate, while the upper BTO layer, being constrained by the lower BTO layer, becomes slightly relaxed in the out-of-plane direction. In addition, the 60 nm buffer sample shows the presence of a Au(111) peak, suggesting that additional orientation of the Au pillars emerges as the buffer layer thickness increases.

Figure 1c presents the XRD plots for frequency dependent samples. The nomenclature "x Hz/y Hz" refers to the laser frequency used for the Au-BTO layer and the BTO-ZnO layer, respectively. Evidently, there is a clear peak splitting in BTO at lower frequencies (2 Hz/2 Hz). Since the diffusion length can be estimated by $x \approx \sqrt{2Dt}$, the adatoms have a longer diffusion length under low frequencies, thus forming a complete coherent interface with STO and becoming more

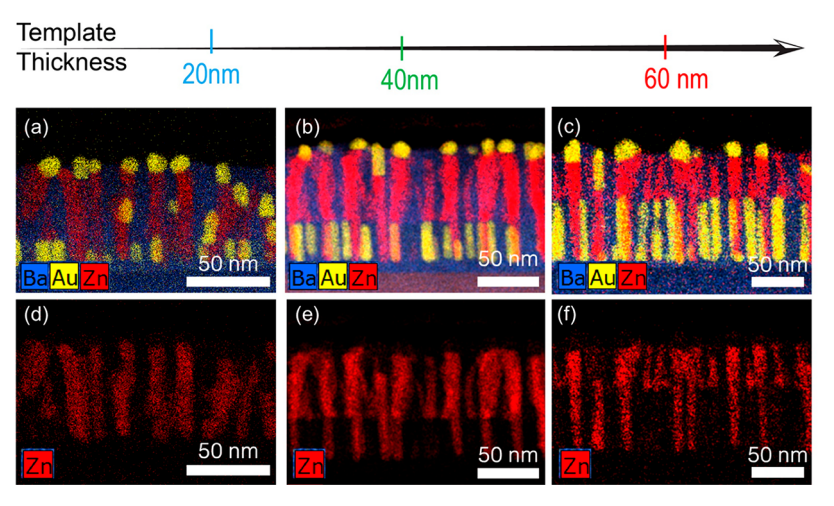


Figure 4. Cross-sectional EDS elemental maps with Au-BTO template thickness, varied from (a) 20 nm, (b) 40 nm, and (c) 60 nm and their corresponding Zn EDS map in (d-f), deposited on STO (001) substrate.

strained. In contrast, the BTO peak splitting becomes less obvious as the two layers are deposited at higher frequencies due to the formation of a semicoherent interface and resulting in strain relaxation. The calculated c lattice parameters of BTO and ZnO for all the samples are presented in Figure 1d with the bulk c lattice parameter marked as a dotted line. Clearly, the BTO and ZnO phase experiences a tensile strain and compressive strain in the out-of-plane direction, respectively. The high epitaxial quality of the samples deposited under two extreme frequencies is further compared using reciprocal space mapping (RSM). Figure 1e,f shows the RSMs near substrate STO (002) peak for the 2 Hz/2 Hz sample and 10 Hz/10 Hz sample, respectively. The c lattice parameter of the lower BTO layer is 4.14 Å and 4.07 Å, while that of the upper BTO layer is 4.07 Å and 4.04 Å, deposited at 2 Hz and 10 Hz, respectively, as calculated from the RSM. This is consistent with the observations in Figure 1c and correspond to the different strain states of the two BTO layers present in the film. In addition, no obvious degradation of the film quality was observed on changing the frequency.

Figure 2a-c shows a collection of EDS elemental maps for samples deposited at 700 °C, 600 °C, and 500 °C, respectively. Figure 2b,c shows the presence of Au NPs at the tip of ZnO NWs, which is indicative of the vapor-liquid-solid (VLS) mechanism. Because of the presence of eutectic solution at 683 °C at 33.5 atom % Zn (L \rightarrow Au + AuZn) in the bulk Au-Zn phase diagram along with a congruently melting AuZn intermetallic,³¹ there must be a presence of ternary eutectic point, assuming the miscibility of ZnO in AuZn intermetallic is almost negligible. Therefore, there must exist a pseudobinary Au-ZnO eutectic system with the eutectic point existing on the Au rich side of the phase diagram.³² Similar pseudobinary systems such as Au-GaAs, Ge-GaSb, Al-Mg₂Si, etc. have been reported earlier. 33-35 Above 600 °C, Au and ZnO form a low melting point eutectic solution which gets supersaturated from the incoming flux of ZnO adatoms to give rise to the uniaxial growth of ZnO nanowires. Clearly, the growth temperatures at 600 and 700 °C show the presence of the VLS mechanism, enabling the formation of the eutectic solution, while the VLS mechanism is absent at 500 °C. Therefore, the growth temperature must be at least above 600 °C for the VLS mechanism to take place.

The effect of growth kinetics on the overall morphology was studied by varying the deposition frequency. Figure 3a-d show a set of EDS maps at different deposition frequencies, i.e., 2 Hz/2 Hz, 2 Hz/10 Hz, 10 Hz/2 Hz, and 10 Hz/10 Hz, respectively. Clearly, all the samples show the presence of Au NP capping the ZnO NW. The EDS elemental map shows the clear and sharp interfaces among Au, BTO, and ZnO, suggesting that all the three phases grow separately without any obvious interdiffusion. The interface between BTO and STO remains largely coherent as seen from the HR-STEM images and their corresponding Fourier-filtered images (shown in Supplementary Figure S1) at 2 Hz and 10 Hz. However, formation of dislocation can be seen in the sample deposited at 10 Hz, resulting in strain relaxation, as observed from the XRD plots earlier. In addition, the deposition kinetics plays a key role in determining the Au and ZnO pillar diameter, and the shape of Au NP. The Au pillar diameter increases from ~7.5 nm to ~10 nm, while the ZnO pillar diameter decreases from \sim 7.6 nm to \sim 5.7 nm at 2 Hz and 10 Hz, respectively. In addition, the aspect ratio (length/height) of the Au NP capping the ZnO NW decreases from ~1.2 at low frequencies to ~0.8 at high frequencies. The large mismatch of Au and ZnO pillar diameter at 10 Hz makes the Au NP aspect ratio <1. Therefore, the relative matching of the ZnO and Au pillar diameter makes it easier for the Au-ZnO system to undergo a VLS mechanism at 2 Hz, which also determines the aspect ratio of the Au NP capping the ZnO nanowire.

The effect of Au-BTO template geometry on the overall morphology was studied by varying the template thickness. Figure 4a-c presents the STEM-EDS images for the 20 nm, 40 nm, and 60 nm Au-BTO template thickness, showing the elemental distribution of Au, BTO, and ZnO phases. As the template thickness is increased from 20 nm to 60 nm, fewer numbers of Au pillars undergo the VLS mechanism. Figure 4d-f shows the EDS mapping of the ZnO phase for the three different template thicknesses. Clearly, the number of ZnO pillars penetrating inside the Au-BTO template layer decreases as the template layer thickness increases. This is due to the relative concentration of Au and ZnO during the deposition. With 20 nm template thickness, there is sufficient concentration of ZnO present to undergo the VLS mechanism with Au pillars. However, as the template thickness increases, some of the ZnO pillars, although being deposited on top of Au

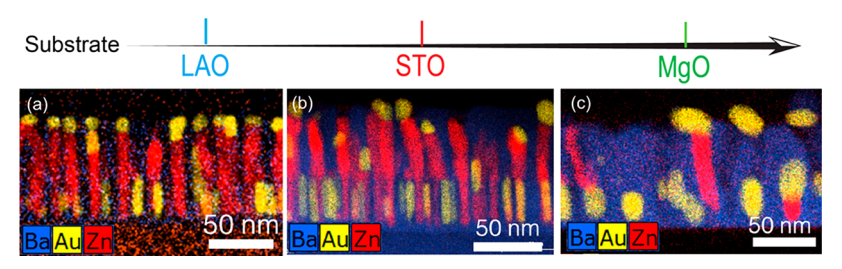


Figure 5. Cross-sectional EDS elemental maps when using different substrates: (a) LaAlO₃ (LAO) (001), (b) STO (001), and (c) MgO (001).

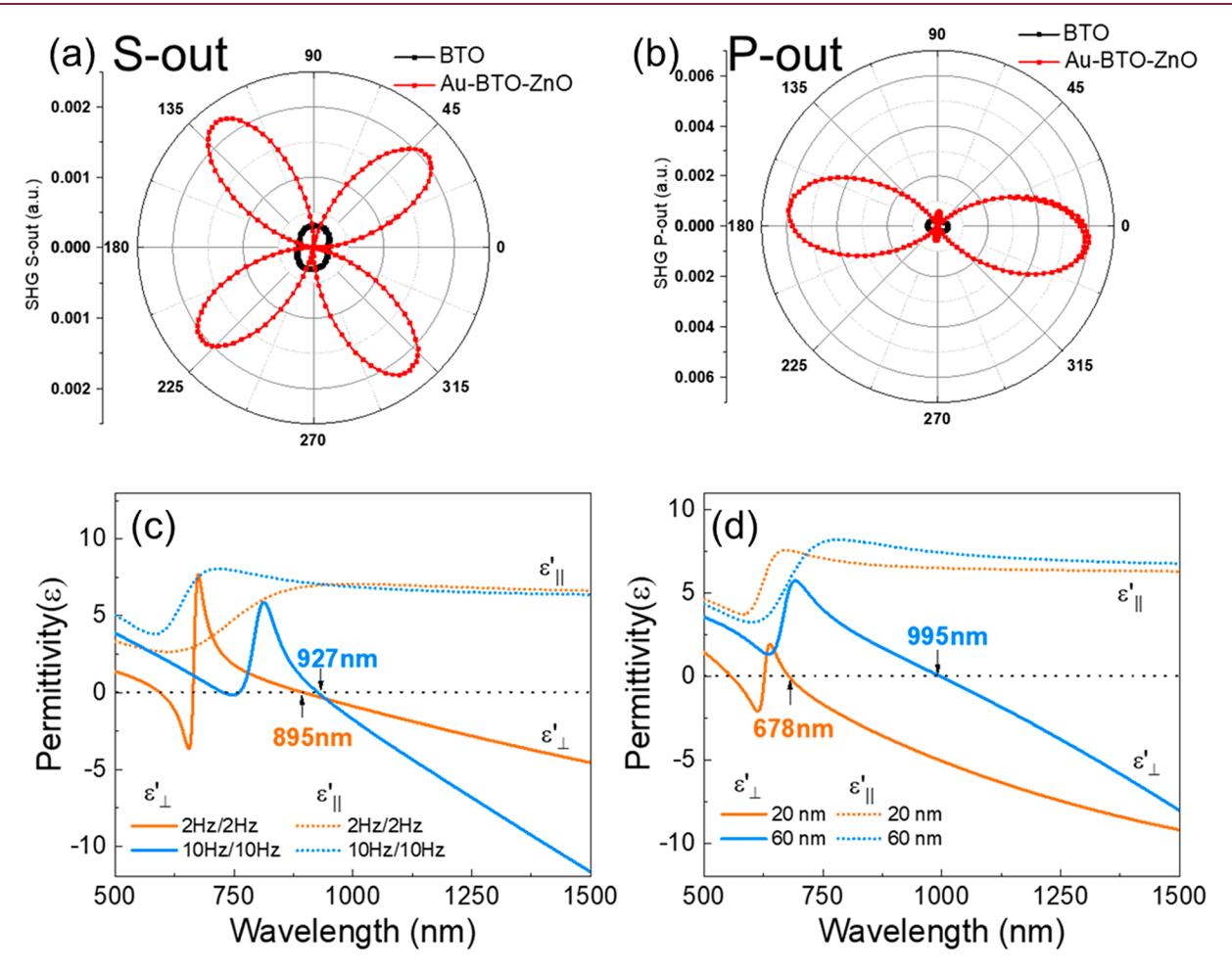


Figure 6. Polar plots of the measured SHG intensity as a function of incident polarization angle with output polarization fixed at (a) 90° (S-out) and (b) 0° (P-out). Real part of the in-plane $(\varepsilon'_{\parallel})$ and out-of-plane (ε'_{\perp}) permittivity at different (c) frequencies and (d) Au-BaTiO₃ template thicknesses, deposited on the STO (001) substrate.

pillars, do not have enough concentration at the Au-ZnO interface to undergo the VLS mechanism with Au. Therefore, tuning the template thickness plays an important role in determining the final morphology of the three-phase nanocomposite.

The effect of strain on the morphology of the three-phase nanocomposite was studied by depositing the films on three different substrates: LAO (001), STO (001), and MgO (001) having a lattice parameter of 3.79 Å, 3.91 Å, and 4.21 Å respectively, which results in a different strain state. All the samples were deposited at 700 °C at 40 mTorr oxygen partial pressure with 10 Hz/2 Hz frequency. Figure S2 (Supporting Information) shows the X-ray diffraction for all the samples. Clearly, BTO shows a highly crystalline and textured (00l) growth. BTO phase experiences a tensile strain of \sim 0.50% on

STO, while it sustains a compressive strain of ~0.50% on both LAO and MgO substrates. Figure 5 compares the microstructure of the three different samples. Overall, the morphology undergoes a change by varying the substrate. The Au pillar diameter varies from ~13 nm (MgO substrate) to ~9 nm (STO substrate) to ~7.5 nm (LAO substrate). The ZnO pillar diameter at 2 Hz is ~8 nm, which matches reasonably well with the Au pillar diameter on STO and LAO substrate. However, there is a large mismatch between the Au and ZnO pillar diameter on MgO, and hence, very few pillars undergo the VLS mechanism resulting in the formation of Au NP on the film surface. In contrast, relatively more Au pillars undergo the VLS mechanism on STO and LAO substrate due to the diameter matching of Au and ZnO.

The following section discusses the tunable optical properties in these three-phase systems with tunable microstructures. First, the nonlinear response of the ordered three-phase sample was measured using the second harmonic generation (SHG). Figure 6a,b presents a polar plot showing the measured SHG intensity as a function of incident light polarization angle with output polarization fixed at 0° (P-out) and 90° (S-out), respectively. An angle resolution of 2° (1° for the half waveplate) was used to scan the input polarization. The SHG intensity of BTO is also plotted for comparison. Clearly, the second-order nonlinearity of the ordered three-phase Au-BTO-ZnO gets enhanced by up to 1 order of magnitude for both 0° and 90° output polarization as compared to the pure BTO film. This enhancement can be attributed to two factors: (i) increased strain state of BTO, and (ii) the interface between Au and BTO. The presence of Au and ZnO, growing vertically in the BTO matrix, results in a higher strained state of BTO up to a greater thickness. In addition, the SHG signal also arises due to the surface nonlinearity at the metal-dielectric interface (Au-BTO interface in this case) as has been observed before.36,37

Second, the optical properties with different deposition parameters were measured. Figure 6c,d shows the optical dielectric permittivity with different deposition frequencies and template thicknesses, respectively, measured using an angulardependent spectroscopic ellipsometer. Because of the anisotropic nature of the nanocomposites, the permittivity was modeled as in-plane $(\varepsilon_{\parallel})$ and out-of-plane (ε_{\perp}) permittivity components using the general oscillator models to make them Kramers-Kronig consistent. Figure 6c compares the dielectric permittivity for the 2 Hz/2 Hz and 10 Hz/10 Hz sample. The in-plane permittivity $(\varepsilon_{\parallel})$ follows similar trends and remains positive throughout the wavelength region. However, the outof-plane permittivity (ε_{\perp}) increases in the visible wavelength region on increasing the frequency from 2 Hz to 10 Hz. In addition, the epsilon-near zero (ENZ) wavelength shows a redshift from 895 nm to 927 nm as the frequency is increased from 2 Hz to 10 Hz. This can be attributed to the lower free electron density in the 10 Hz sample. Figure 6d compares the dielectric permittivity for the 20 nm and 60 nm template thickness. Again, the in-plane permittivity for both the samples shows similar trends and remains positive throughout the wavelength regime. Interestingly, the out-of-plane permittivity shows a clear red-shift in the ENZ wavelength from 678 nm to 995 nm as the template thickness increases, implying that the sample with the thinner template is more metallic. Owing to the higher free electron density, the 20 nm template thickness sample shows a blue-shift in the ENZ wavelength. The 20 nm sample also exhibits negative out-of-plane permittivity in the visible wavelength region due to presence of a greater amount of Au NP as compared to the 60 nm sample. Therefore, by tuning the template geometry as well as the deposition kinetics, the optical response of the three-phase nanocomposite can be successfully tuned.

Tuning the deposition parameters such as growth temperature, deposition frequency and template thickness provides extra degrees of freedom to tune the microstructure and its corresponding optical properties. For example, maintaining the growth temperature above a critical temperature leads to the activation of the VLS mechanism. Such a study also helps understand the diffusion kinetics during the growth process. Specifically, optimization of the relative Au and ZnO pillar diameter leads to an ordered growth of the three-phase

nanocomposite as shown by varying the deposition frequency and substrate-induced in-plane strain.

In addition, microstructure evolution tunes the ENZ wavelength, which is important for achieving nonlinear optical response in different wavelength regimes. The ENZ wavelength tunability is achieved over a larger wavelength range from $\sim\!650$ nm to $\sim\!1000$ nm compared to those achieved previously. These tuning effects can be attributed to the relative change in the free electron density. The increased nonlinearity of the three-phase sample is also confirmed by the enhanced SHG response. Therefore, this study provides an opportunity to tune the microstructure and physical properties of three-phase metal—dielectric nanocomposite systems which can be extended to other two-phase and three-phase systems.

CONCLUSIONS

In summary, the morphology tuning of the three-phase nanocomposite of Au-BTO-ZnO by varying the growth temperature, deposition frequency, and template thickness has been presented as an effective approach in achieving tunable microstructure and optical properties. The growth temperature above 600 °C shows the presence of Au NP capping the ZnO NW, indicative of the VLS mechanism. Increasing the template thickness decreases the number of ZnO pillars undergoing the VLS mechanism. Varying the frequency of the Au-BTO template and BTO-ZnO layer results in microstructure evolution, which is mainly driven by the relative matching of the Au and ZnO pillar diameter. Such microstructure evolution in these hyperbolic metamaterials tunes the free electron density in the out-of-plane direction, thereby tuning the ENZ wavelength in the Z-direction. This study demonstrates the great potential in tunable, three-phase nanocomposite systems meeting various optical device needs.

■ EXPERIMENTAL DETAILS

Thin Film Growth. The self-assembled, three-phase Au-BTO-ZnO nanocomposite thin films were deposited using a two-step growth using a Au-BTO buffer layer as a template as shown previously. First, a buffer layer of Au-BTO layer was deposited (using a Au-BTO composite target) followed by the deposition of BTO-ZnO layer (using a BTO-ZnO composite target). The thin films were deposited on STO (001), MgO (001), LAO (001) single-crystal substrates using pulsed laser deposition (PLD) (with a KrF excimer laser, Lambda Physik Compex Pro 205, $\lambda=248$ nm). All the films were deposited at 40 mTorr oxygen pressure in the temperature range of 400–700 °C and in the frequency range of 2–10 Hz.

Structural and Optical Characterization. The microstructure of the films were characterized using XRD (PANalytical Empyrean XRD) and high-resolution STEM (FEI TALOS 200X operated at 200 kV). Cross-section TEM samples were prepared using the manual grinding, polishing, and thinning process followed by dimpling and ion milling using precision ion polishing system (PIPS II, Gatan). The SHG measurements were carried out using a home-built system with an amplified Ti:sapphire laser. The dielectric permittivity of the films was measured using a spectroscopic ellipsometer (JA Woollam RC2).

ASSOCIATED CONTENT

Solution Supporting Information

The Supporting Information is available free of charge at https://pubs.acs.org/doi/10.1021/acs.cgd.0c00801.

BTO-STO interface as a function of frequency, XRD of three-phase nanocomposite on different substrates (PDF)

AUTHOR INFORMATION

Corresponding Author

Haiyan Wang — School of Materials Engineering and School of Electrical and Computer Engineering, Purdue University, West Lafayette, Indiana 47907, United States; orcid.org/0000-0002-7397-1209; Email: hwang00@purdue.edu

Authors

- Shikhar Misra School of Materials Engineering, Purdue
 University, West Lafayette, Indiana 47907, United States
- Di Zhang School of Materials Engineering, Purdue University, West Lafayette, Indiana 47907, United States
- **Zhimin Qi** School of Materials Engineering, Purdue University, West Lafayette, Indiana 47907, United States
- Dongfang Li Center for Integrated Nanotechnologies, Los Alamos National Laboratory, Los Alamos, New Mexico 87545, United States
- Juanjuan Lu School of Materials Engineering, Purdue University, West Lafayette, Indiana 47907, United States
- **Hou-Tong Chen** Center for Integrated Nanotechnologies, Los Alamos National Laboratory, Los Alamos, New Mexico 87545, United States; Occid.org/0000-0003-2014-7571

Complete contact information is available at: https://pubs.acs.org/10.1021/acs.cgd.0c00801

Notes

The authors declare no competing financial interest.

ACKNOWLEDGMENTS

The work was partially supported by the U.S. Department of Energy, Office of Science, Basic Energy Science under Award DE-SC0020077. The high resolution TEM/STEM imaging effort was funded by the U.S. National Science Foundation (DMR-1565822 and DMR-2016453). S.M. acknowledges the support from the Bilsland Dissertation Fellowship. D.Z. acknowledges the support from the Office of Naval Research under Contract N00014-17-1-2087 and N00014-20-1-2043. This work was performed, in part, at the Center for Integrated Nanotechnologies, an Office of Science User Facility.

■ REFERENCES

- (1) Huang, J.; Jin, T.; Misra, S.; Wang, H.; Qi, Z.; Dai, Y.; Sun, X.; Li, L.; Okkema, J.; Chen, H.; Lin, P.; Zhang, X.; Wang, H. Tailorable Optical Response of Au–LiNbO₃ Hybrid Metamaterial Thin Films for Optical Waveguide Applications. *Adv. Opt. Mater.* **2018**, *6*, 1800510.
- (2) Jian, J.; Wang, X.; Misra, S.; Sun, X.; Qi, Z.; Gao, X.; Sun, J.; Donohue, A.; Lin, D. G.; Pol, V.; Youngblood, J.; Wang, H.; Li, L.; Huang, J.; Wang, H. Broad Range Tuning of Phase Transition Property in VO₂ Through Metal-Ceramic Nanocomposite Design. *Adv. Funct. Mater.* **2019**, 29, 1903690.
- (3) Kawasaki, S.; Takahashi, R.; Yamamoto, T.; Kobayashi, M.; Kumigashira, H.; Yoshinobu, J.; Komori, F.; Kudo, A.; Lippmaa, M. Photoelectrochemical water splitting enhanced by self-assembled metal nanopillars embedded in an oxide semiconductor photoelectrode. *Nat. Commun.* **2016**, *7*, 11818.
- (4) Misra, S.; Li, L.; Jian, J.; Huang, J.; Wang, X.; Zemlyanov, D.; Jang, J.-W.; Ribeiro, F. H.; Wang, H. Tailorable Au Nanoparticles Embedded in Epitaxial TiO₂ Thin Films for Tunable Optical Properties. ACS Appl. Mater. Interfaces 2018, 10, 32895.
- (5) Qi, Z.; Jian, J.; Huang, J.; Tang, J.; Wang, H.; Pol, V. G.; Wang, H. LiNi_{0.5}Mn_{0.3}Co_{0.2}O₂/Au nanocomposite thin film cathode with enhanced electrochemical properties. *Nano Energy* **2018**, 46, 290.

- (6) Schio, P.; Vidal, F.; Zheng, Y.; Milano, J.; Fonda, E.; Demaille, D.; Vodungbo, B.; Varalda, J.; De Oliveira, A. J. A.; Etgens, V. H. Magnetic response of cobalt nanowires with diameter below 5 nm. *Phys. Rev. B: Condens. Matter Mater. Phys.* **2010**, 82, 094436.
- (7) Weng, X.; Hennes, M.; Coati, A.; Vlad, A.; Garreau, Y.; Sauvage-Simkin, M.; Fonda, E.; Patriarche, G.; Demaille, D.; Vidal, F.; Zheng, Y. Ultrathin Ni nanowires embedded in SrTiO₃: Vertical epitaxy, strain relaxation mechanisms, and solid-state amorphization. *Phys. Rev. Mater.* **2018**, *2*, 106003.
- (8) Zhang, B.; Huang, J.; Jian, J.; Rutherford, B. X.; Li, L.; Misra, S.; Sun, X.; Wang, H. Tuning magnetic anisotropy in Co-BaZrO₃ vertically aligned nanocomposites for memory device integration. *Nanoscale Adv.* **2019**, *1*, 4450.
- (9) Zhang, D.; Misra, S.; Li, L.; Wang, X.; Jian, J.; Lu, P.; Gao, X.; Sun, X.; Qi, Z.; Kalaswad, M.; Zhang, X.; Wang, H. Tunable Optical Properties in Self-Assembled Oxide-Metal Hybrid Thin Films via Au-Phase Geometry Control: From Nanopillars to Nanodisks. *Adv. Opt. Mater.* **2020**, *8*, 1901359.
- (10) Vidal, F.; Zheng, Y.; Schio, P.; Bonilla, F. J.; Barturen, M.; Milano, J.; Demaille, D.; Fonda, E.; De Oliveira, A. J. A.; Etgens, V. H. Mechanism of localization of the magnetization reversal in 3 nm wide Co nanowires. *Phys. Rev. Lett.* **2012**, *109*, 117205.
- (11) Su, Q.; Zhang, W.; Lu, P.; Fang, S.; Khatkhatay, F.; Jian, J.; Li, L.; Chen, F.; Zhang, X.; MacManus-Driscoll, J. L.; Chen, A.; Jia, Q.; Wang, H. Self-Assembled Magnetic Metallic Nanopillars in Ceramic Matrix with Anisotropic Magnetic and Electrical Transport Properties. ACS Appl. Mater. Interfaces 2016, 8, 20283.
- (12) Li, L.; Sun, L.; Gomez-Diaz, J. S.; Hogan, N. L.; Lu, P.; Khatkhatay, F.; Zhang, W.; Jian, J.; Huang, J.; Su, Q.; Fan, M.; Jacob, C.; Li, J.; Zhang, X.; Jia, Q.; Sheldon, M.; Alù, A.; Li, X.; Wang, H. Self-assembled epitaxial Au-oxide vertically aligned nanocomposites for nanoscale metamaterials. *Nano Lett.* **2016**, *16*, 3936.
- (13) Zhang, B.; Huang, J.; Rutherford, B.; Lu, P.; Misra, S.; Kalaswad, M.; He, Z.; Gao, X.; Sun, X.; Li, L.; Wang, H. Tunable room temperature multiferroic Fe-BaTiO₃ vertically aligned nanocomposite with perpendicular magnetic anisotropy. *Mater. Today Nano* 2020, 11, 100083.
- (14) Qi, Z.; Tang, J.; Misra, S.; Fan, C.; Lu, P.; Jian, J.; He, Z.; Pol, V. G.; Zhang, X.; Wang, H. Enhancing electrochemical performance of thin film lithium ion battery via introducing tilted metal nanopillars as effective current collectors. *Nano Energy* **2020**, *69*, 104381.
- (15) Narimanov, E. E.; Kildishev, A. V. Naturally hyperbolic. *Nat. Photonics* **2015**, *9*, 214.
- (16) Zhang, X.; Liu, Z. Superlenses to overcome the diffraction limit. *Nat. Mater.* **2008**, *7*, 435.
- (17) Zhang, S.; Fan, W.; Panoiu, N. C.; Malloy, K. J.; Osgood, R. M.; Brueck, S. R. J. Experimental Demonstration of Near-Infrared Negative-Index Metamaterials. *Phys. Rev. Lett.* **2005**, *95*, 137404.
- (18) Pendry, J. B. Negative Refraction Makes a Perfect Lens. *Phys. Rev. Lett.* **2000**, *85*, 3966.
- (19) Huang, J.; Qi, Z.; Li, L.; Wang, H.; Xue, S.; Zhang, B.; Zhang, X.; Wang, H. Self-assembled vertically aligned Ni nanopillars in CeO_2 with anisotropic magnetic and transport properties for energy applications. *Nanoscale* **2018**, *10*, 17182.
- (20) Huang, J.; Li, L.; Lu, P.; Qi, Z.; Sun, X.; Zhang, X.; Wang, H. Self-assembled $Co-BaZrO_3$ nanocomposite thin films with ultra-fine vertically aligned Co nanopillars. *Nanoscale* **2017**, *9*, 7970.
- (21) Paldi, R. L.; Sun, X.; Wang, X.; Zhang, X.; Wang, H. Strain-Driven In-plane Ordering in Vertically Aligned ZnO-Au Nano-composites with Highly Correlated Metamaterial Properties. *ACS Omega* **2020**, *5*, 2234.
- (22) Huang, J.; Wang, X.; Phuah, X. L.; Lu, P.; Qi, Z.; Wang, H. Plasmonic Cu nanostructures in ZnO as hyperbolic metamaterial thin films. *Mater. Today Nano* **2019**, *8*, 100052.
- (23) Rashed, A. R.; Gudulluoglu, B.; Yun, H. W.; Habib, M.; Boyaci, I. H.; Hong, S. H.; Ozbay, E.; Caglayan, H. Highly-Sensitive Refractive Index Sensing by Near-infrared Metatronic Nanocircuits. *Sci. Rep.* **2018**, *8*, 11457.

- (24) Nasir, M. E.; Dickson, W.; Wurtz, G. A.; Wardley, W. P.; Zayats, A. V. Hydrogen detected by the naked eye: Optical hydrogen gas sensors based on core/shell plasmonic nanorod metamaterials. *Adv. Mater.* **2014**, *26*, 3532.
- (25) Fang, N.; Lee, H.; Sun, C.; Zhang, X. Sub-Diffraction-Limited Optical Imaging with a Silver Superlens. *Science* **2005**, *308*, 534.
- (26) Poddubny, A.; Iorsh, I.; Belov, P.; Kivshar, Y. Hyperbolic metamaterials. *Nat. Photonics* **2013**, *7*, 948.
- (27) Valentine, J.; Li, J.; Zentgraf, T.; Bartal, G.; Zhang, X. An optical cloak made of dielectrics. *Nat. Mater.* **2009**, *8*, 568.
- (28) Caspani, L.; Kaipurath, R. P. M.; Clerici, M.; Ferrera, M.; Roger, T.; Kim, J.; Kinsey, N.; Pietrzyk, M.; Di Falco, A.; Shalaev, V. M.; Boltasseva, A.; Faccio, D. Enhanced Nonlinear Refractive Index in ϵ -Near-Zero Materials. *Phys. Rev. Lett.* **2016**, *116*, 233901.
- (29) Alam, M. Z.; De Leon, I.; Boyd, R. W. Large optical nonlinearity of indium tin oxide in its epsilon-near-zero region. *Science* **2016**, 352, 795.
- (30) Misra, S.; Li, L.; Zhang, D.; Jian, J.; Qi, Z.; Fan, M.; Chen, H.; Zhang, X.; Wang, H. Self-Assembled Ordered Three-Phase Au–BaTiO₃–ZnO Vertically Aligned Nanocomposites Achieved by a Templating Method. *Adv. Mater.* **2019**, *31*, 1806529.
- (31) Okamoto, H.; Massalski, T. B. The Au-Zn (Gold-Zinc) system. Bull. Alloy Phase Diagrams 1989, 10, 59.
- (32) Borchers, C.; Muller, S.; Stichtenoth, D.; Schwen, D.; Ronning, C. Catalyst Nanostructure Interaction in the Growth of 1-D ZnO Nanostructures. *J. Phys. Chem. B* **2006**, *110*, 1656.
- (33) Shah, S. I.; Cadien, K. C.; Greene, J. E. GaSb-Ge pseudobinary phase diagram. *J. Electron. Mater.* 1982, 11, 53.
- (34) Zhang, J.; Fan, Z.; Wang, Y. Q.; Zhou, B. L. Equilibrium pseudobinary Al Mg₂Si phase diagram. *Mater. Sci. Technol.* **2001**, *17*, 494.
- (35) Duan, X.; Lieber, C. M. General Synthesis of Compound Semiconductor Nanowires. *Adv. Mater.* **2000**, *12*, 298.
- (36) Nireekshan Reddy, K.; Chen, P. Y.; Fernández-Domínguez, A. I.; Sivan, Y. Revisiting the boundary conditions for second-harmonic generation at metal-dielectric interfaces. *J. Opt. Soc. Am. B* **2017**, *34*, 1824.
- (37) Cao, L.; Panoiu, N. C.; Osgood, R. M. Surface second-harmonic generation from surface plasmon waves scattered by metallic nanostructures. *Phys. Rev. B: Condens. Matter Mater. Phys.* **2007**, 75, 205401.